# Weakly pinned skyrmion liquid in a magnetic heterostructure

Rhodri Mansell [1,*] Yifan Zhou,[1] Kassius Kohvakka,[1] See-Chen Ying [2], Ken R. Elder,[3] Enzo Granato [4], Tapio Ala-Nissila,[5,6] and Sebastiaan van Dijken [1]

[1]*NanoSpin, Department of Applied Physics, Aalto University School of Science, P.O. Box 15100, FI-00076 Aalto, Finland*
[2]*Department of Physics, Brown University, P.O. Box 1843, Providence, Rhode Island 02912-1843, USA*
[3]*Department of Physics, Oakland University, Rochester. Michigan 48309, USA*
[4]*Laboratório Associado de Sensores e Materiais, Instituto Nacional de Pesquisas Espaciais, 12227-010 São José dos Campos, SP, Brazil*
[5]*QTF Center of Excellence, Department of Applied Physics, Aalto University, FI-00076 Aalto, Espoo, Finland*
[6]*Interdisciplinary Centre for Mathematical Modelling and Department of Mathematical Sciences, Loughborough University, Loughborough, Leicestershire LE11 3TU, United Kingdom*

Magnetic skyrmions are topologically distinct particles whose thermally activated motion could be used to implement probabilistic computing paradigms. While solid-liquid phase transitions in skyrmion lattices have been demonstrated, the behavior of a skyrmion liquid and the effects of pinning are largely unknown. Here we demonstrate the formation of a weakly pinned skyrmion liquid in a magnetic heterostructure. By inserting a Ru wedge layer at the ferromagnet/heavy metal interface we evaluate the dependence of skyrmion dynamics on the skyrmion size and density. Our experiments demonstrate that the diffusion of skyrmions is largest in dense liquids with small skyrmions. The thermal motion of skyrmions at room temperature easily overcomes the narrow distribution of pinning site energies in the granular film structure, satisfying a key requirement of probabilistic device architectures. Micromagnetic simulations support the findings and also reveal the existence of a thermally activated high-frequency collective oscillation.

## I. INTRODUCTION

Magnetic skyrmions [1,2] occur in a wide range of magnetic systems [3–7]. The small size and stability of skyrmions combined with the ability to drive them with electrical currents has led to interest in using them in memory and logic devices [1,8,9]. As emergent particles, skyrmions can also undergo thermally excited diffusion [7,10], which for most device proposals would reduce the device effectiveness. As an alternative, devices which exploit thermal motion to implement nonconventional computing paradigms, such as probabilistic computing, have been proposed [10–12]. The thermally excited motion of individual skyrmions has been experimentally studied [10,13], along with multiple skyrmions in confined geometries [14]. The implementation of skyrmion diffusion-based devices in ultrathin films will require an in-depth understanding of the interaction between skyrmions and the material grains and pinning sites commonly found in such films [15–17]. The interaction of skyrmions with such defects has so far been studied using molecular dynamic and micromagnetic simulations [18,19], as well as through the combination of experimental and simulation work [20,21].

Along with the possibility of making devices, the intrinsic behavior of skyrmions is of great interest. Most device proposals require skyrmions to be metastable excitations, but skyrmions can also be the lowest energy state of a system leading to the formation of skyrmion lattices [22]. It has been demonstrated that a lattice of skyrmions can melt from a crystalline phase to a liquid phase passing through a hexatic phase [7,23,24]. However, the behavior of skyrmions in a liquid phase, and, in particular, in the presence of pinning sites, has not been well studied. Here we study the thermally activated motion of dipole-stabilized magnetic bubble skyrmions [25] in an ultrathin magnetic heterostructure with perpendicular anisotropy [3,26]. The size and density of skyrmions is controlled by a Ru insertion layer. We demonstrate that the skyrmions form a weakly pinned liquid at room temperature [27], and extract the correlation lengths and correlation times of skyrmions in the liquid. Furthermore, we investigate the pinning of skyrmions, finding that there is a narrow and spatially uncorrelated distribution of pinning strengths. The experimental results are well approximated by suitable micromagnetic simulations, which also reveal the existence of a thermally excited high frequency collective oscillation mode of the skyrmions, which may be relevant for high frequency devices.

## II. THEORETICAL BACKGROUND

The motion of a skyrmion under an applied force can be approximately described by the Thiele equation [28], which assumes that the skyrmions have a rigid spin structure:

$$M_s \gamma^{-1} \boldsymbol{G} \times \dot{\boldsymbol{C}} + M_s \gamma^{-1} \alpha \mathcal{D} \dot{\boldsymbol{C}} = \boldsymbol{F}, \tag{1}$$
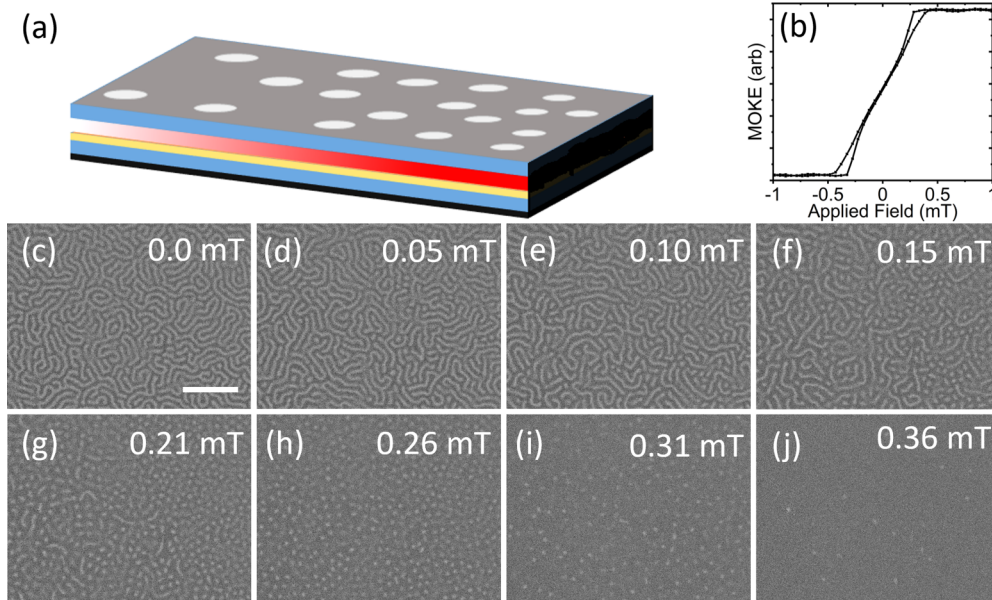
*rhodri.mansell@aalto.fi

054413-1

FIG. 1. (a) Schematic of the Ta/Pt/CoFeB/Ru wedge/Pt multilayer sample. (b) Perpendicular MOKE measurement of the sample under out-of-plane applied fields at the same position (V) on the wedge as the following images. The MOKE signal is averaged over the $88 \times 67$ $\mu m^2$ image. (c)–(j) Polar MOKE microscopy images showing magnetic contrast at one position on the wedge as a function of applied magnetic field, with (c) 0.0 mT, (d) 0.05 mT, (e) 0.10 mT, (f) 0.15 mT, (g) 0.21 mT, (h) 0.26 mT, (i) 0.31 mT, and (j) 0.36 mT. The scale bar in (c) is 20 $\mu$m in length. All images are at the same scale.

where $M_s$ is the saturation magnetization, $\gamma$ is the gyromagnetic ratio, $\alpha$ is the magnetic damping constant, $\boldsymbol{G} = (0, 0, G)$ is the gyromagnetic coupling vector where $G = \pm 4\pi$ for a skyrmion, $\boldsymbol{C}(t)$ is the center-of-mass coordinate of the skyrmion, $\mathcal{D}$ is known as the dissipative force tensor, and $\boldsymbol{F}$ is an applied force (see methods for details). The first term on the left-hand side of Eq. (1) gives the gyrotropic motion of skyrmions, which causes them to move orthogonally to an applied force. This term has significant effects on skyrmion behavior. For instance, it has been shown that the gyrotropic component reduces the effectiveness of point pinning sites [16], and leads to motion along a magnetic anisotropy boundary [17,29].

The thermally driven dynamics of individual skyrmions have been extensively studied both in experiments and in simulations. Theoretically, it is expected that individual skyrmions in the absence of pinning sites follow Brownian motion with a diffusivity D given by [30,31]

$$ \mathsf{D} = k_\mathrm{B} T \frac{\alpha \mathcal{D}}{G^2 + (\alpha \mathcal{D})^2}, \tag{2} $$

where $k_\mathrm{B}$ is Boltzmann's constant, and $T$ is the temperature. For a typical set of material parameters, the effect of the gyrotropic motion is to cause the diffusivity to increase as the magnetic damping increases [31], the opposite of what might be expected. Through the dissipative force tensor this equation has a dependence on the skyrmion radius and spin profile [31]. However, Eq. (2) only applies to an isolated single skyrmion on a smooth film, and the skyrmion behavior is likely to be modified in the presence of an interacting array of skyrmions, as well as in the presence of pinning sites [19].

## III. RESULTS

In Fig. 1(a) we show a schematic of the sample. It consists of a Ta/Pt/CoFeB/Ru wedge/Pt multilayer (see methods for details), where the Ru insertion layer alters the properties of the magnetic layer. In previous work we have shown that a Pt underlayer in combination with a Ru insertion layer separating the CoFeB and top Pt layer induces a considerable Dzyaloshinskii-Moriya interaction [26] which stabilizes skyrmions. Magneto-optical Kerr effect (MOKE) microscopy is used to image the magnetization state of the sample, with videos of the sample being taken at six positions along the Ru wedge and at a series of different applied fields (see methods).

In Fig. 1(b) a MOKE hysteresis loop for one position on the wedge is shown, which is anhysteretic at lower fields with some hysteresis before saturation. In Figs. 1(c)–1(j) we show the detailed changes in the magnetization of the sample at a particular position on the wedge. The images are taken after applying an AC field during which a background image is taken, which is then subtracted to show only the magnetic contrast. This also leads to a consistent domain state for applied magnetic fields in the hysteretic part of the loop (see methods for details). Starting from a stripe domain state at very low applied magnetic fields [Figs. 1(c) and 1(d)], an increasing field leads to the progressive collapse of stripe domains into skyrmions. From 0.10 to 0.21 mT skyrmions coexist with stripe domains with the fraction of skyrmions increasing with increasing field [Figs. 1(e)–1(g)]. At 0.26 mT a pure skyrmion state appears with a skyrmion density of 0.11 skyrmions/$\mu m^2$ [Fig. 1(g)]. At higher fields the skyrmions become sparser until only a small number are visible in the field of view at 0.36 mT [Fig. 1(i)]. The change from a
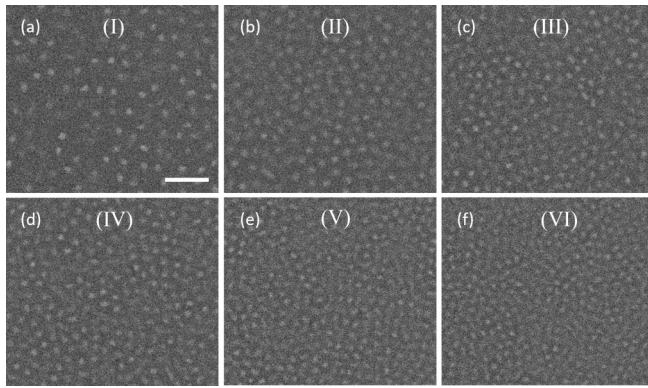
FIG. 2. MOKE microscopy images of the skyrmion state at 0.26 mT applied out-of-plane field for different thicknesses of the Ru wedge. The positions are referred to in the text using Roman numerals. For increasing Ru thickness the skyrmion densities in skyrmions/$\mu$m$^2$ are (a) 0.07 (I), (b) 0.11 (II), (c) 0.15 (III), (d) 0.13 (IV), (e) 0.17 (V), and (f) 0.20 (VI). The scale bar indicates 10 $\mu$m.

stripe domain to a field-induced skyrmion bubble phase is well established in thin films of this type [3,13,26]. Images of the skyrmion phases at 0.26 mT applied field at the six different positions on the wedge used in this paper are shown in Fig. 2. The centers of the positions are 100 $\mu$m apart. As the Ru wedge increases in thickness from position (I) to position (VI) the skyrmions become smaller and denser. The change in Ru thickness across the six positions is of the order of 0.1 nm, showing the sensitivity of the domain structure to small changes. This sensitivity is likely due to the reduction in perpendicular magnetic anisotropy and increase in DMI that come from the substitution of Ru for Pt at the interface. The data presented in the paper are collected at room temperature, due to the large changes in the magnetic domain state for small changes in temperature as show in the Supplemental Material Fig. S1 [32].

### A. Static structure

Video stills at position (II) are shown in Fig. 3(a) at zero magnetic field and at 0.26 mT applied field in Fig. 3(b), where a skyrmion phase with a density of 0.11 skyrmions/$\mu$m$^2$ is seen. For a thicker Ru insertion layer [position (V)] the stripe domains at zero field become narrower [Fig. 3(c)] and the skyrmion phase at 0.26 mT [Fig. 3(d)] consists of smaller and denser skyrmions (0.17 skyrmions/$\mu$m$^2$). There is a strong correlation between the size and density of the skyrmions, which is shown in the Supplemental Material Fig. S2 [32]. The insets in Figs. 3(a)–3(d) show the static structure functions which are derived from the spatial Fourier transform of the images (see methods) and particularly contain information about intermediate length scales. For a crystalline arrangement of skyrmions an ordered array of peaks showing long-range order would be expected. For a liquid or glass with only short-range order a ring is expected with no preferential direction. A gaslike phase would give a broad peak around the origin. Here the single ring indicates the dominance of a single length scale in the ordering of the magnetic domains and skyrmions. Some angular modulation is visible for the
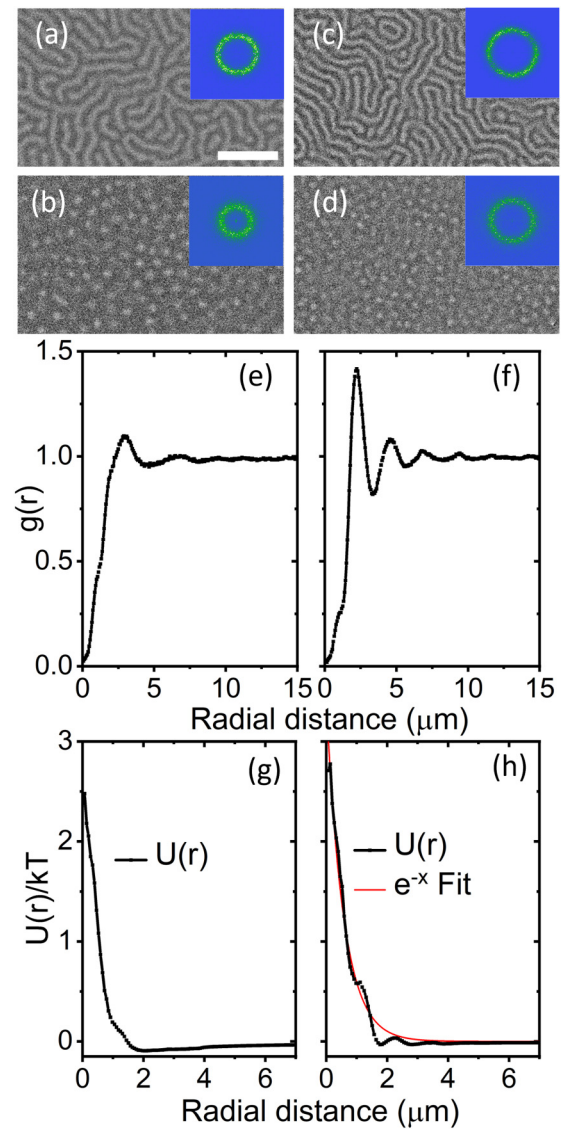


FIG. 3. (a) Zero-magnetic field MOKE microscopy image showing a stripe domain pattern at position (II). The scale bar indicates 20 $\mu$m. (b) At the same position (II) as (a) a skyrmion array with a density of 0.11 skyrmions/$\mu$m$^2$ forms in 0.26 mT applied field. (c) and (d) are as (a) and (b) but at position (V) where the skyrmion array has a density of 0.17 skyrmions/$\mu$m$^2$. The insets in (a)–(d) show the static structure functions of the microscopy images. (e) Radial pair distribution function for the skyrmion arrays at 0.26 mT at position (II) and (f) position (V). (g) Skyrmion-skyrmion pair interaction derived from the skyrmion arrays at 0.26 mT at position (II) and (h) position (V).

stripe domains, indicating a weak preferential direction, but the skyrmion phases are circularly symmetric, which is typical of liquid or glassy phases where no preferential direction is expected [7,33].

In Figs. 3(e) and 3(f) the radial pair distribution functions $g(r)$ of the skyrmion phases in Figs. 3(b) and 3(d) are shown (see methods). This contains information on the average distance between particles, as well as whether it is a gas, liquid/glass, or crystalline phase. For the larger and sparser skyrmions in Fig. 3(b) a clear initial peak is seen
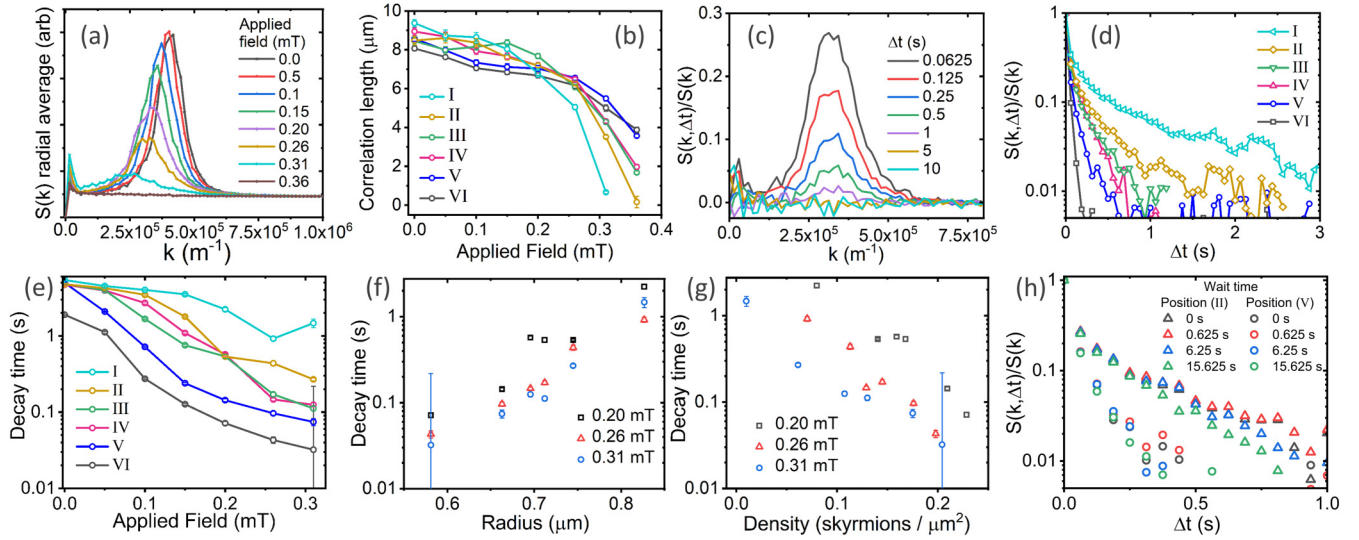
FIG. 4. (a) Radially averaged static structure functions at position (II) for different applied magnetic fields, corresponding to the images shown in Fig. 1. (b) Correlation length as a function of applied magnetic field at the six sample positions with different Ru thickness. (c) Normalized intermediate scattering function as a function of wave vector, shown for different lag times, $\Delta t$ at position (II). (d) Normalized intermediate scattering function against lag time at 0.26 mT applied field for the six sample positions. (e) Decay time of the intermediate scattering function peak at the six sample positions as a function of applied magnetic field. (f) Decay time of the intermediate scattering function peak as a function of skyrmion radius. (g) Decay time of the intermediate scattering function peak as a function of skyrmion density. (h) Dependence of the normalized intermediate scattering time on a wait time for positions (II) and (V).

followed by a few significantly weaker peaks as the radial distance increases before the signal decays to the average background level [Fig. 3(e)]. This behavior is as expected for a liquid/glass phase. For the smaller and denser skyrmions in Fig. 3(d) multiple peaks are clearly visible in the radial pair distribution function in Fig. 3(f), indicating the presence of correlations in the positions of skyrmions over a much longer length scale than the average distance between particles. This data can be used to gain information about the interactions between particles, as well. Using the hypernetted chain closure for the Ornstein-Zernike equation (see methods) we can extract the skyrmion-skyrmion pair interaction $U(r)$, shown in Figs. 3(g) and 3(h) [34]. An approximately exponential decay of the interaction strength with distance is expected theoretically and from simulations [11,35,36], which is consistent with what is seen here. Interestingly, despite differences in the radius and density of the skyrmions the decay lengths of the exponential part of the pair interaction are similar, at around 1 $\mu$m (see also the Supplemental Material Fig. S3 [32]), at all positions of the wedge and for different applied magnetic fields. There are also extra oscillations superimposed on the decaying exponential, particularly visible in Fig. 3(h). An oscillation in the skyrmion-skyrmion interaction has also been predicted from atomic simulations [35]. In the same way that the stripe domain state has a periodicity given by the competing exchange, DMI and dipolar interactions, combined with the external magnetic field, the skyrmion-skyrmion interaction may also have a local minimum reflecting this competition. That the long-range dipolar interaction is likely to play a role in determining the average spacing of the skyrmions in this system means that the extracted $U(r)$ here is unlikely to be the same as that extracted from studying the interaction of a pair of skyrmions directly [36].

By taking the radial average of the static structure functions more quantitative information can be obtained. Figure 4(a) shows the radially averaged static structure functions at position (II). The peaks are well fitted by a Lorentzian line shape which reduces in height and broadens with increasing field. These changes indicate the reducing order of the magnetic state. However, the transition from a stripe domain state to a skyrmion state around 0.20 mT does not lead to any marked changes. For applied field values near saturation, the skyrmions are sparse which leads to a gaslike structure function with a peak at the smallest wave vector as seen for the data at 0.36 mT [33].

By fitting a Lorentzian peak to the structure functions derived at the six sample positions for different fields, the correlation lengths can be extracted (see methods), as shown in Fig. 4(b). The correlation lengths describe how far across the sample a change in magnetization will lead to a corresponding change at another position. At zero field the lowest energy state of the system has no net magnetization and is characterized by stripe domains of a width determined by the magnetic parameters, meaning that thermally induced changes in magnetization at one point lead to correlated changes over multiple stripe domain widths [37,38]. As the field is increased the correlation lengths decrease but again there is no clear transition from stripe domains to skyrmions in the data. There is also surprisingly little variation in the correlation length at a given applied field even though there is a greater than factor of 2 variation in the skyrmion density at different positions. For higher fields, where the skyrmions are relatively sparse, the correlation length drops rapidly. For these fields, the large average distance between skyrmions leads to a weak skyrmion-skyrmion interaction and the correlation length becomes similar to the skyrmion size.

## B. Dynamic properties

As well as the static structural properties, the stripe domains and skyrmions show thermally activated movement. In the Supplemental Videos [32] the motion of both the stripe domain states and the skyrmions arrays is shown. As seen in Fig. 3, the azimuthal dependence of the static structure functions is weak for the stripe domains and there is no azimuthal dependence for the skyrmion states. Therefore, in order to capture the domain motion we use the normalized radially averaged intermediate scattering functions (see methods) which contains information about the space and time dependence of correlations in the system. In particular, it can describe the extent of the similarity of the system as a function of the lag time. In Fig. 4(c) we show the intermediate scattering function of the skyrmion state at 0.26 mT at position (II) as a function of lag time between video frames. The data consist of a single broad peak centered around the same wave vector as the static structure function [Fig. 4(a)] whose intensity decays with increasing lag time. The decays of the correlations with the lag time for the six different wedge positions and 0.26 mT applied field is shown in Fig. 4(d). The decays consist of an initial drop followed by a slower decay which is roughly exponential. This exponential part depends strongly on the position along the wedge.

The equivalent decay times for all six sample positions as a function of magnetic field are shown together in Fig. 4(e), fitted as a double exponential where the longer decay constant is shown. We observe two main features. First, the decay time decreases roughly exponentially with increasing field, without a discontinuity when the magnetic stripe domains transition into a skyrmion array. Second, the decay time reduces for denser stripe domains and smaller/denser skyrmions.

These observations are quantified in Figs. 4(f) and 4(g) where a strong dependence of the scattering function decay on the skyrmion radius and skyrmion density is shown. In both cases a roughly exponential relationship is seen with decreasing radius and increasing density leading to faster decay times.

The intermediate scattering function in Fig. 4(d) can be fitted with a stretched exponential function typical of systems with depinning from traps. This fitting is summarized in the Supplemental Material Fig. S4 [32], and suggests that such a fitting leads to a low stretching exponent which could be consistent with a glassy as opposed to liquid state. In a glassy state the sample would be expected to undergo aging shown by the slowing of the decay of the intermediate scattering function for increasing wait times after initialization [39]. To test this, in Fig. 4(h) the decay as a function of a wait time is shown for positions (II) and (V), where the decay remains similar for all the wait times tested. For position (V) the maximum wait time is around two orders of magnitude larger than the decay time strongly suggesting that the system does not show aging.

## C. Pinning

Thus far we considered the macroscopic properties of mobile skyrmions arrays. It is clear from the videos of the skyrmions that microscopic interactions with pinning sites play an important role in the behavior of the system. In Figs. 5(a)–5(e) a few skyrmions at the same position are shown as a function of time at position (V). The skyrmions
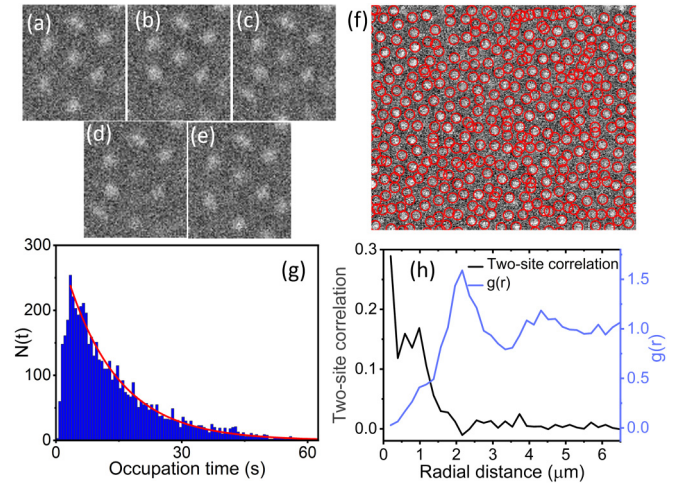


FIG. 5. (a)–(e) Images of a few skyrmions at position (V) at different times. (f) Extracted pinning sites from averaged video stills, a whiter color within the red circle indicates greater occupation of a site. (g) Histogram of skyrmion occupation time calculated using $8 \times 8$ pixel areas. (h) Two-site correlation function calculated using the pinning probability (left-hand axis) plotted with the radial pair distribution function (right-hand axis). See text for details.

at the top of the image are strongly pinned. At the bottom of the image the skyrmions engage in a series of interconnected jumps between well-defined positions. In ultrathin sputtered heterostructures as studied here there are material grains due to the polycrystalline growth of the Ta/Pt underlayers. From x-ray diffraction measurements on a similar sample to the one measured here the grain size is determined to be ∼11 nm (see the Supplemental Material Fig. S5 [32]) in line with similar sputtered multilayer samples [40]. Other forms of a pinning site are possible, such as point defects, but the existence of grains provides a parsimonious explanation for the pinning. Due to the size of the grains, individual skyrmions interact with a large number of grains.

In Fig. 5(f) the positions of pinning sites at the same location are extracted from time-averaged video stills. The whiter the color within the red circle the longer a skyrmion occupied the pinning site. Note that circles can overlap, meaning that there are multiple possible sites in less than the average skyrmion radius as also seen in Figs. 5(a)–5(e).

Figure 5(g) shows a histogram of the occupation time for skyrmions calculated using $8 \times 8$ pixel areas (see methods), which shows an exponential decay of the number of sites as the occupation time increases (red fit line). In a simple two state classical Boltzmann model the dwell time in one state is expected to be exponentially distributed. That the distribution of skyrmion occupation times shows an exponential decay therefore indicates that there is a fairly narrow distribution of pinning site energies. To test whether there is any pattern to the strength of the pinning sites, the correlation between pinning strengths can be calculated. Using the pinning sites identified in Fig 5(f), the probability of depinning between video frames is calculated (see methods). In Fig. 5(h) a radial distance dependent two-site correlation function is plotted (left axis) along with the pair distribution function (right axis) plotted for comparison (see methods). The correlation

function measures the similarity in pinning strength between neighboring pinning sites. It shows a rapid decrease in the correlation for small distances, such that at the first peak of the pair distribution function $g(r)$ there is no correlation between the strength of neighboring pinning sites. At larger distances, therefore, the strength of pinning sites is randomly distributed. The existence of a notable correlation at short distances is likely due to closely spaced weak pinning sites, which skyrmions rapidly move between. Some examples of such closely spaced weak pinning sites are seen in Fig. 5(f), particularly in the top right of the image.

### D. Micromagnetic simulations

To understand better the experimental data we use micromagnetic simulations to investigate the behavior of skyrmions interacting with a material grain structure. We use similar parameters to those expected for the film studied here, taken from a previous similar sample [26] (see also methods). In Fig. 6(a) a snapshot of a micromagnetic simulation is shown, carried out at an effective temperature of 300 K, and with an out-of-plane field of 160 mT. With these conditions skyrmions nucleate spontaneously leading to a skyrmion density of $\sim$320 skyrmions/$\mu$m$^2$ after a short relaxation time. The simulation includes a grain structure of 10 nm average diameter with a corresponding variation in the magnetic anisotropy (as a Gaussian distribution with a standard deviation of 5%) and DMI (as a Gaussian distribution with a standard deviation of 15%). The skyrmions are both thermally excited into motion and interact with the grains [19]. Although similar material parameters are used as in the experiments, the skyrmions in the simulations are significantly smaller, with an average radius around 14 nm, and the relevant timescales are orders of magnitude shorter. The reason for this discrepancy is unclear, although it may relate to the difficulty of reproducing the experimental dipolar fields. The inset in Fig. 6(a) shows the static structure function which is dominated by a single ring. The simulations also reveal a skyrmion-skyrmion interaction potential similar to the experiments (see Fig. S6 in the Supplemental Material [32]). The dynamic properties given by the normalized intermediate scattering function are shown in Fig. 6(b). Simulations allow much shorter time steps relative to the skyrmion motion. A broad peak is seen at short times which rapidly decays at longer times, resembling the data in Fig. 4(c). The shorter time steps also mean that individual skyrmions can be reliably tracked, allowing the extraction of more information than is available in the experimental case. In Fig. 6(c) we show the self-intermediate scattering function (see methods), which is extracted by tracking the paths of individual skyrmions through the simulation at different wave vectors. Following a short initial decay, there is an exponential decay of the correlations which for larger wave vectors then levels off at longer lag times. This behavior at long lag times is absent in a simulation carried out without grains (see the Supplemental Material Fig. S7 [32]). The mean square displacement $\langle \Delta r^2 \rangle$ of the simulated skyrmions can also be extracted as shown in Fig. 6(d). For simple Brownian diffusion the mean square displacement is expected to increase linearly with lag time $\Delta t$, as shown by the line with a slope of 1. The extracted curve shows a notable deviation
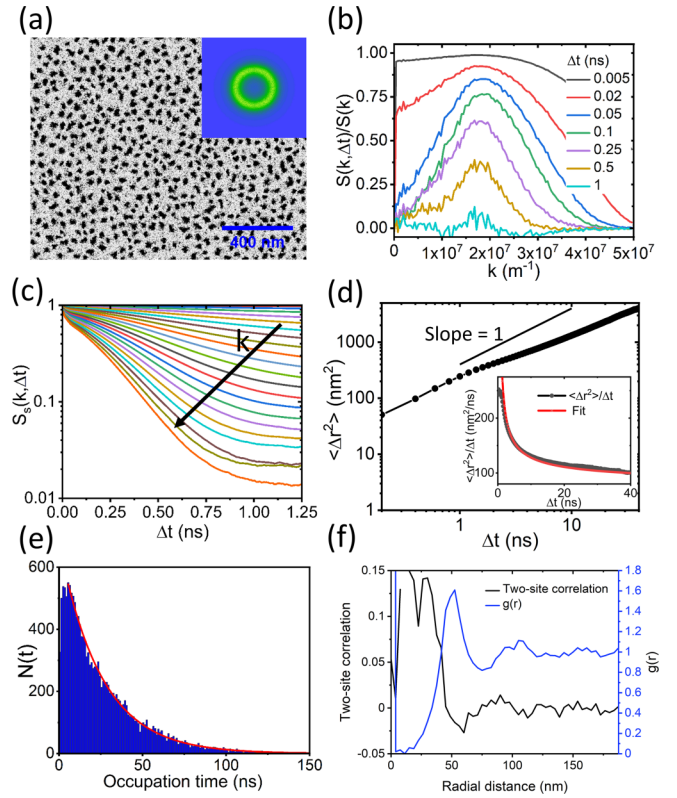


FIG. 6. (a) Snapshot of part of a micromagnetic simulation at 160 mT applied field. Inset shows the static structure function. (b) Intermediate scattering function as a function of momentum for different delay times. (c) Self-intermediate scattering function as a function of delay time $k$ increases in the direction of the arrow from $2.7 \times 10^6$ to $5.0 \times 10^7$ m$^{-1}$ in steps of $2.4 \times 10^6$ m$^{-1}$. (d) Mean square displacement of the skyrmions $\langle \Delta r^2 \rangle$ as a function of lag time $\Delta t$. The inset shows $\langle \Delta r^2 \rangle / \Delta t$, which is fitted to $D_0[1 + 4/\ln(\Delta t)]$ where $D_0$ is the diffusion coefficient. (e) Histogram of skyrmion occupation time calculated using $8 \times 8$ pixel areas. (f) Two-site correlation function calculated using the pinning probability (left-hand axis) plotted with the radial pair distribution function (right-hand axis).

at lag times greater than 1 ns, with the slope increasing again at longer lag times. The grains in the simulation act as weak pinning sites which alters the diffusion of the skyrmions. In two-dimensional diffusion with weak pinning and spatial correlations that rapidly decay, Bouchaud and Georges [41] show that the mean squared displacement is given by $\langle \Delta r^2(\Delta t) \rangle \sim 2D_0 \Delta t (1 + 4/\ln \Delta t)$ where $D_0$ is the diffusion coefficient. In the inset we plot $\langle \Delta r^2(\Delta t) \rangle / \Delta t$, which shows the correction to the standard Brownian motion, and a fit to the $1 + 4/\ln(\Delta t)$ term. The good fit suggests that the assumptions underlying the theory are well met in this case.

Following on from this, in Fig. 6(e) the distribution of pinning times is shown, which has an exponentially decaying number of sites with increasing pinning time, similar to Fig. 5(g). In Fig. 6(f) a similar correlation function to the experimental pattern is also shown for the case of pinning in the simulations.

Experimentally the strong temperature dependence of the magnetic parameters prevents us from studying the
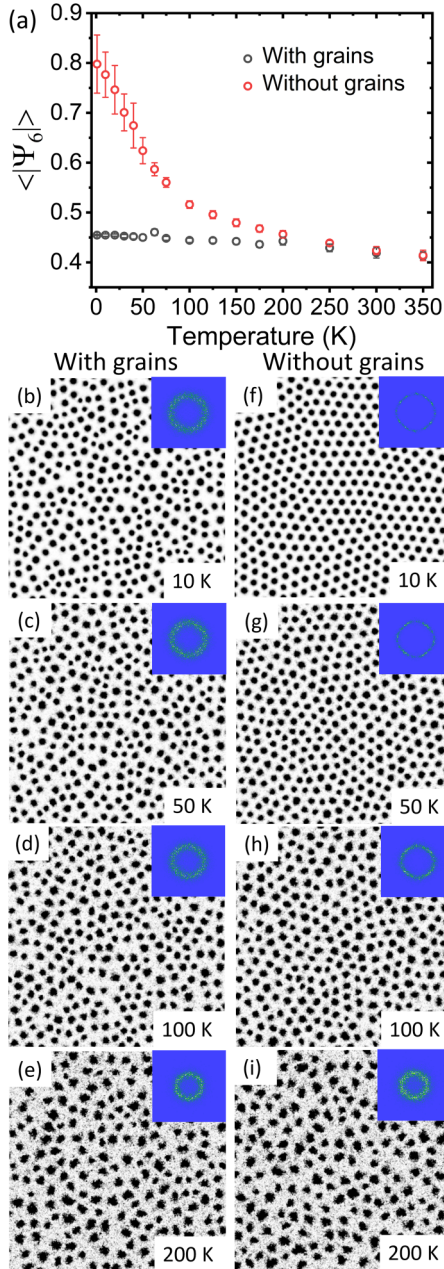
FIG. 7. (a) The sixfold bond-orientational order parameter calculated for simulations with (black) and without (red) pinning as a function of temperature. Magnetization snapshots from simulations as a function of temperature with grains at (b) 10 K, (c) 50 K, (d) 100 K, (e) 200 K and without grains at (f) 10 K, (g) 50 K, (h) 100 K, (i) 200 K. The insets show the static structure function.

temperature dependence of thermally driven skyrmion dynamics. Using simulations, however, the temperature can be varied while keeping all the magnetic parameters constant. In Fig. 7(a) we compare the effect of changing the temperature in simulations with and without a grain structure. We characterize the system with a sixfold bond order parameter (see methods), which indicates the extent of the orientational ordering in the system. Snapshots of the simulations at different temperatures with grains are shown in Figs. 7(b)–7(e) and without grains in Figs. 7(f)–7(i). At high temperatures the two
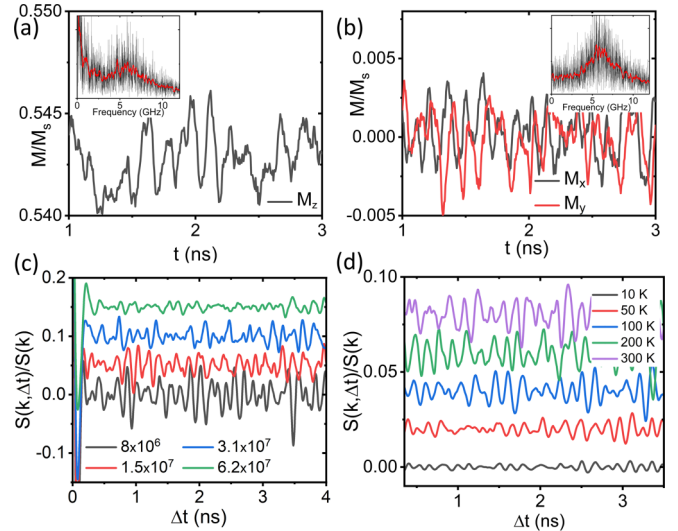


FIG. 8. (a) The time dependence of $M_z$ spatially averaged across the simulation. The inset shows the FFT of the data (black) with a Savitsky-Golay average (red). (b) The time dependence of $M_x$ (black) and $M_y$ (red) spatially averaged across the simulation. The inset shows the FFT of the $M_x$ data (black) with a Savitsky-Golay average (red). (c) The detrended intermediate scattering function at four different particular wave vectors at 300 K. The curves are offset for clarity. (d) The detrended intermediate scattering function as a function of temperature at a wave vector of $4 \times 10^6$ m$^{-1}$.

simulations both show low sixfold order indicating the formation of a liquid phase, with little difference between the two simulations shown in Figs. 7(e) and 7(i). As the temperature is reduced in the simulation without grains, the orientational order of the system increases steadily, forming a state with a high degree of order at lower temperatures [Figs. 7(f) and 7(g)]. For the simulations with a grain structure a very small increase of the ordering of skyrmions is seen with reducing temperature [see Figs. 7(b)–7(d)] and it clearly diverges from the case without grains at less than 200 K.

### E. High frequency collective mode

In the simulations, a synchronized oscillation in the skyrmion size can be seen (shown in the Supplemental Video 4 [32]). In Fig. 8(a) the normalized magnetic moment in the simulation, averaged over the entire area, is shown. There are clear periodic oscillations which give a broad peak in the Fourier transform of the data shown in the inset at around 6 GHz. In Fig. 8(b) we show the fractional change in the in-plane magnetization in the x and y directions where it can be seen that the oscillations occur with a lag between the $M_x$ and $M_y$ components. Therefore, this skyrmion behavior is related to both an oscillation of the skyrmion size and gyrotropic motion of the skyrmions [42]. Figure 8(c) shows the detrended normalized intermediate scattering functions (see methods) for four wave vectors, showing that the magnitude of the oscillation decays with increasing wave vector. That the oscillation is strongest at low wave vectors demonstrates that this is a collective oscillation of the sample. In Fig. 8(d) we show the temperature dependence of the oscillation at fixed wave vector also by plotting the detrended normalized intermediate scattering

scattering function. While the oscillation is already present at 10 K, it rapidly increases in amplitude up to 100 K and then remains roughly the same at higher temperatures. Such long-range synchronized oscillations are likely to be mediated by dipole fields, with neighboring skyrmions also being affected by changing skyrmion-skyrmion interactions. The existence of a collective thermal excitation of skyrmions is important because it may affect the behavior of proposed devices based on the nonlinear response of skyrmions to currents [11,43] or open routes to novel high-frequency devices.

## IV. DISCUSSION

The skyrmion layers measured here have the structure expected of a liquid or glass, showing short-range order in dense arrays. To distinguish between a liquid and glass we need to understand the details of the dynamics of the skyrmion arrays. In the simulations, the system is clearly in a liquid state at 300 K, as the simulations with and without grains are identical above 200 K as shown in Fig. 7. Despite this the interaction of skyrmions with grains still alters the motion of the skyrmions and the associated correlation functions as shown in Fig. 6. The experimental data in Fig. 4(d) can also be fitted using the stretched exponential form often used for glasses (see the Supplemental Material Fig. S4 [32]) [44], however the simulation data suggest such altered correlations exist for the liquid case too. One glasslike property that can be tested is aging for which we find no evidence as shown in Fig. 4(h). Together this suggests that the skyrmions are in a liquid state where the correlation functions are modified by the pinning—a weakly pinned liquid.

The properties of the skyrmion liquid depend on the interaction of three energy scales, the thermal energy, the pinning, and the skyrmion-skyrmion interaction. In sputtered thin films, such as the one studied here, the grains which lead to pinning largely arise from the Ta/Pt underlayers [40] and so it is expected that the pinning sites are similar for all the points on the wedge. In the experimental film, the skyrmions are weakly pinned and the arrays have the structure expected of a liquid, but the temporal correlations do not completely decay at long times due to the presence of preferential pinning sites. This is also seen in the simulation results, where, once the temperature is raised above a certain level, the structure of the liquid does not depend on the pinning sites, even though the skyrmions are still weakly pinned. In denser arrays the skyrmion-skyrmion interaction is also important. Experimentally, as the density increases, the correlation times decrease, which is probably due to an increase of the skyrmion-skyrmion interaction energy relative to the pinning energy.

The possibility of tuning the desired static and dynamic properties of skyrmion arrays will enhance the feasibility of producing stochastic computation devices. This tuning can be achieved through modifying the magnetic parameters, or through modifying the grains—for instance through ion bombardment [45]. The behavior of the skyrmions can be modeled using micromagnetic simulations with a grain structure and a thermal field. The grain structure of the polycrystalline film leads to pinning sites with a narrow energy distribution as seen in the experiments. The relatively small distribution of pinning

energies is of interest for applications of a wide variety of skyrmion devices as it suggests that devices incorporating pinning due to grains are still viable for current-driven devices. Lastly, the existence of a thermally activated collective breathing and gyrotropic mode may also be relevant when designing stochastic devices that operate at higher frequencies [46] and highlights an important gap in our knowledge of skyrmion properties.

## V. METHODS

### A. Thiele equation

The Thiele equation [28] decomposes the motion of a rigid skyrmion under an applied force into two terms. The spin structure of a skyrmion is assumed to be rigid, so that by defining $\boldsymbol{r}$ as the position vector of the spins relative to the skyrmion center and $\boldsymbol{C}(t)$ as the center-of-mass coordinate of the skyrmion, we obtain $\boldsymbol{m}(\boldsymbol{r}, t) = \boldsymbol{m}[\boldsymbol{r} - \boldsymbol{C}(t)]$. The dynamics of a magnetic skyrmion structure can then be described by the Thiele equation [2,28,47]

$$M_s \gamma^{-1} \boldsymbol{G} \times \dot{\boldsymbol{C}} + M_s \gamma^{-1} \alpha \mathcal{D} \dot{\boldsymbol{C}} = \boldsymbol{F}, \qquad (3)$$

where

$$G = \iint dx dy \, \boldsymbol{m} \cdot \left( \frac{\partial \boldsymbol{m}}{\partial x} \times \frac{\partial \boldsymbol{m}}{\partial y} \right),$$

$$\mathcal{D} = \iint dx dy \frac{\partial \boldsymbol{m}}{\partial x} \cdot \frac{\partial \boldsymbol{m}}{\partial y},$$

$$\boldsymbol{F} = -\nabla U. \qquad (4)$$

Here $\nabla U$ is the energy gradient within a skyrmion, and $\boldsymbol{F}$ is the equivalent driving force. $\boldsymbol{G} = (0, 0, G)$ is the gyromagnetic coupling vector where $G = \pm 4\pi$ for a skyrmion. $\mathcal{D}$ is called the dissipative force tensor. $M_s$ is the saturation magnetization and $\gamma$ is the gyromagnetic ratio.

### B. Film growth

The sample consists of a Ta $(2\,\text{nm})$/Pt $(4\,\text{nm})$/ $Co_{0.4}Fe_{0.4}B_{0.2}$ $(0.8\,\text{nm})$/Ru wedge/Pt $(4\,\text{nm})$ heterostructure grown by magnetron sputtering in a chamber with a base pressure of $5 \times 10^{-8}$ mbar. The Ru wedge is created using the movement of a shutter. On the thin side of the wedge, the Ru is around 0.2 nm thick and along the wedge the thickness increases by around 0.1 nm across the studied area.

### C. MOKE microscopy

Magneto-optical Kerr effect (MOKE) microscopy is carried out on a Evico system based on a Zeiss microscope, using a $100\times$ lens in a polar MOKE configuration. The lens has a numerical aperture of 0.8, which combined with the white light source gives a resolution of $\sim 400$ nm. Videos of 1000 frames of $672 \times 512$ pixels were taken at 16 frames per second using a Hamamatsu C4742-95 digital camera, giving an imaged area of $88 \times 67 \,\mu\text{m}^2$. The six positions from which data are collected have a center-to-center spacing of 100 $\mu$m. A composite image of an area similar to the one used in the experiments is shown in the Supplemental Material Fig. S1 [32]. A Helmholtz coil is used to apply an out-of-plane magnetic field. The magnetic state is initialized by setting the magne-

tic field to the required DC value with an additional 1 mT AC field. During application of the AC field a background image is taken which is then subtracted from the image to leave only magnetic contrast. The AC field then decays over 5 s to leave just the DC field. The video acquisition is then started.

### D. Experimental structure functions

From the experimental MOKE microscopy images, the static structure function and the intermediate scattering function are calculated. The static structure function is given by

$$S(\boldsymbol{k}) = \langle \rho_k \rho_{-k} \rangle, \tag{5}$$

where $\rho_k$ is the 2D spatial Fourier transform of the MOKE microscopy video images. For both the static and dynamic structure functions a $512 \times 512$ window in the center of the image is used. The angle brackets indicate an ensemble average. The intermediate scattering function, which gives time dependent changes, is calculated using

$$S(\boldsymbol{k}, \Delta t) = \langle \rho_k(t) \rho_{-k}(t + \Delta t) \rangle_t - \langle \rho_k(t) \rangle \langle \rho_{-k}(t + \Delta t) \rangle_t, \tag{6}$$

where $\Delta t$ is the time lag between frames and the ensemble average is taken over the time, $t$.

### E. Correlation length

The static structure functions at different positions and applied magnetic fields can be fitted by a Lorentzian of the form:

$$S(k) = \frac{2A}{\pi} \frac{\xi}{4(k - x_0)^2 + 1/\xi^2} + y_0, \tag{7}$$

where $A$ is a scaling factor, $x_0$ is the wave vector of the peak, $\xi$ is the correlation length, and $y_0$ is a vertical offset.

### F. Radial pair distribution function

The radial pair distribution function is given by

$$g(r) = \frac{1}{2\pi r} \frac{1}{N\rho} \sum_{i=1}^{N} \sum_{k \neq i}^{N} \langle \delta(\boldsymbol{r} - |\boldsymbol{r}_k - \boldsymbol{r}_i|) | \rangle, \tag{8}$$

where $r$ is the radial distance, $N$ is the number of skyrmions, $\rho$ is the skyrmion density, and $\boldsymbol{r}_i$ is the position of a skyrmion. The positions of the skyrmions are extracted from the MOKE microscopy videos using the TrackMate plugin of ImageJ [48]. The radial pair distribution function is calculated for each frame and then averaged to obtain the presented data.

### G. Skyrmion-skyrmion pair interaction

The pair interaction can be calculated using the hypernetted chain closure:

$$U(r) = -\ln[g(r)] + h(r) - c(r), \tag{9}$$

where $g(r)$ is the pair distribution function, $h(r) = g(r) - 1$, and $c(r)$ is the Fourier transform of $\tilde{c}(k)$ defined by the Ornstein-Zernike equation as

$$\tilde{c}(k) = \frac{\tilde{h}(k)}{1 + \rho_0 \tilde{h}(k)}, \tag{10}$$

where $\tilde{h}(k)$ is the Hankel transform of $h(r)$ and $\rho_0$ is the areal density of skyrmions.

### H. Areal distribution of pinning sites and probability of depinning

For Fig. 5(f) we use the TrackMate plugin of ImageJ [48] in order to identify typical skyrmion positions in the time averaged video sequence. These positions are then plotted on the averaged image as a red circle with 6 pixel radius. Then by averaging the intensity for $5 \times 5$ pixels around the selected positions, the intensity as a function of time around each point is extracted from the videos, which is thresholded to convert it into data giving the presence or absence of a skyrmion as a function of time at a particular site. Using a simple two-site Markov model, we extract the probability of the skyrmion remaining on the site from one frame to the next. In order to study the correlations between sites we use a method similar to the method used to extract the pair distribution function (see above), however since we use long-time averaged data the function is different to that extracted in Fig. 3. For each skyrmion position the distance to all other skyrmions positions is found. The probability interval of [0 1] for the skyrmion staying on a site is linearly converted to a $[-1 \ 1]$ interval in order to calculate the correlation as a function of distance $C(r)$, given by

$$C(r) = \langle P(R)P(R + r) \rangle - \langle P(R) \rangle \langle P(R + r) \rangle, \tag{11}$$

where $P(R)$ is the converted probability at site $R$. For Fig. 5(g) the skyrmion positions in each video frame are extracted using the TrackMate plugin of ImageJ [48]. The video frame are then divided into $8 \times 8$ pixel areas and the total time any skyrmion is present in each $8 \times 8$ region is calculated. The data then plotted as a histogram of the number of $8 \times 8$ areas that have a particular total occupation time.

### I. Micromagnetic simulations

Micromagnetic simulations are carried out using the Mu-Max3 code [49,50]. The following parameters are used, saturation magnetization $M_s = 9.0 \times 10^5$ A/m, exchange length $A_{\mathrm{ex}} = 6.5 \times 10^{-12}$ J/m, interfacial DMI $D = 1.7 \times 10^{-3}$ J/m$^2$, uniaxial anisotropy $K_u = 6.0 \times 10^5$ J/m$^3$. The data presented in the main paper uses an applied out-of-plane magnetic field of 160 mT. Grains were created using a Voronoi code with an average size of 10 nm [51]. The variation in the local parameters was drawn from a Gaussian distribution with a standard deviation of 5% for $K_u$ and 15% for $D$. The parameters are adapted from a detailed study on similar films [26], although the values of $M_s$ and $D$ are slightly increased. This leads to significantly smaller skyrmions than seen experimentally so that the simulations encompass a larger number of skyrmions with significant mobility on a length scale and timescale that is accessible to micromagnetic simulations. The simulations use a $1024 \times 1024$ grid with 2.5 nm spacing in the $x$ and $y$ direction and with a 0.8 nm thick magnetic layer in the $z$ direction. Thermal effects are simulated using a random thermal field which updates on each time step [49]. For the data in Figs. 6(a)–6(c) a sequence of 1600 magnetization configurations are saved at a $5 \times 10^{-12}$ s time interval, while

Figs. [6(d)]–[6(f)] uses the same simulation parameters but with 1000 frames extracted at intervals of 0.2 ns. Figure [7] uses 25 frames taken 1 ns apart.

### J. Structure functions derived from micromagnetic simulations

The static structure function and the intermediate scattering function can be calculated from images of the magnetization from the simulations in the same way as for the experimental data described above. For the simulation data, however, it is also possible to track the movement of individual skyrmions. However, oscillations in the size of the skyrmions, and the fact that skyrmions annihilate and nucleate during the simulation, limit the duration of skyrmion tracking. For tracking we use scripts based on the trackpy module for python [52]. The individual trajectories can then be used to produce the self-intermediate scattering function by calculating

$$S_s(\boldsymbol{k}, \Delta t) = \frac{1}{N} \left\langle \sum_{j=1}^{N} \exp\{i\boldsymbol{k} \cdot [\boldsymbol{r}_j(t + \Delta t) - \boldsymbol{r}_j(t)]\} \right\rangle_t, \quad (12)$$

where $\boldsymbol{r}_j(t)$ is the position of the skyrmion at time $t$. The ensemble average is taken over all tracked skyrmions and times. By fitting the exponential decay of this function at larger times, the decay time as a function of wave vector can be obtained. For Brownian motion it is expected that:

$$S_s(k, \Delta t) = \exp[-Dk^2 t], \quad (13)$$

### K. Sixfold bond orientational order

In Fig. [7(a)] we use the sixfold bond orientational order parameter to provide a measure of the ordering of the skyrmions in the simulations. The parameter is defined as

$$\Psi_6(k) = \frac{1}{N_k} \sum_{l=1}^{N_k} e^{i6\theta_{kl}}, \quad (14)$$

where the calculation sums over the angles between the $k$th skyrmion and its nearest neighbors, defined by a Voronoi partitioning of the space. We then plot the average of the real part of $\Psi_6$ for all skyrmions.

### ACKNOWLEDGMENTS

[1] A. Fert, V. Cros, and J. Sampaio, Nat. Nanotechnol. **8**, 152 (2013).

[2] N. Nagaosa and Y. Tokura, Nat. Nanotechnol. **8**, 899 (2013).

[3] W. Jiang, P. Upadhyaya, W. Zhang, G. Yu, M. B. Jungfleisch, F. Y. Fradin, J. E. Pearson, Y. Tserkovnyak, K. L. Wang, O. Heinonen, S. G. Te Velthuis, and A. Hoffmann, Science **349**, 283 (2015).

[4] X. Z. Yu, N. Kanazawa, Y. Onose, K. Kimoto, W. Z. Zhang, S. Ishiwata, Y. Matsui, and Y. Tokura, Nat. Mater. **10**, 106 (2011).

[5] P. Milde, D. Köhler, J. Seidel, L. M. Eng, A. Bauer, A. Chacon, J. Kindervater, S. Mühlbauer, C. Pfleiderer, S. Buhrandt, C. Schütte, and A. Rosch, Science **340**, 1076 (2013).

[6] W. Legrand, D. Maccariello, F. Ajejas, S. Collin, A. Vecchiola, K. Bouzehouane, N. Reyren, V. Cros, and A. Fert, Nat. Mater. **19**, 34 (2020).

[7] P. Huang, T. Schönenberger, M. Cantoni, L. Heinen, A. Magrez, A. Rosch, F. Carbone, and H. M. Rønnow, Nat. Nanotechnol. **15**, 761 (2020).

[8] R. Tomasello, E. Martinez, R. Zivieri, L. Torres, M. Carpentieri, and G. Finocchio, Sci. Rep. **4**, 6784 (2015).

[9] X. Zhang, M. Ezawa, and Y. Zhou, Sci. Rep. **5**, 9400 (2015).

[10] J. Zázvorka, F. Jakobs, D. Heinze, N. Keil, S. Kromin, S. Jaiswal, K. Litzius, G. Jakob, P. Virnau, D. Pinna, K. Everschor-Sitte, L. Rózsa, A. Donges, U. Nowak, and M. Kläui, Nat. Nanotechnol. **14**, 658 (2019).

[11] D. Pinna, F. Abreu Araujo, J.-V. Kim, V. Cros, D. Querlioz, P. Bessiere, J. Droulez, and J. Grollier, Phys. Rev. Applied **9**, 064018 (2018).

[12] Y. Jibiki, M. Goto, E. Tamura, J. Cho, S. Miki, R. Ishikawa, H. Nomura, T. Srivastava, W. Lim, S. Auffret, C. Baraduc, H. Bea, and Y. Suzuki, Appl. Phys. Lett. **117**, 082402 (2020).

[13] T. Nozaki, Y. Jibiki, M. Goto, E. Tamura, T. Nozaki, H. Kubota, A. Fukushima, S. Yuasa, and Y. Suzuki, Appl. Phys. Lett. **114**, 012402 (2019).

[14] C. Song, N. Kerber, J. Rothörl, Y. Ge, K. Raab, B. Seng, M. A. Brems, F. Dittrich, R. M. Reeve, J. W. Q. Liu, P. Virnau, and M. Kläui, Adv. Funct. Mater., **31**, 2010739 (2021).

[15] S.-Z. Lin, C. Reichhardt, C. D. Batista, and A. Saxena, Phys. Rev. B **87**, 214419 (2013).

[16] C. Reichhardt, D. Ray, and C. J. Olson Reichhardt, Phys. Rev. Lett. **114**, 217202 (2015).

[17] A. Salimath, A. Abbout, A. Brataas, and A. Manchon, Phys. Rev. B **99**, 104416 (2019).

[18] C. Reichhardt, C. J. O. Reichhardt, and M. V. Milosevic, arXiv:2102.10464.

[19] Y. Zhou, R. Mansell, T. Ala-Nissila, and S. van Dijken, Phys. Rev. B **104**, 144417 (2021).

[20] C. Hanneken, A. Kubetzka, K. von Bergmann, and R. Wiesendanger, New J. Phys. **18**, 055009 (2016).

[21] K. Zeissler, M. Mruczkiewicz, S. Finizio, J. Raabe, P. M. Shepley, A. V. Sadovnikov, S. A. Nikitov, K. Fallon, S. McFadzean, S. McVitie, T. A. Moore, G. Burnell, and C. H. Marrows, Sci. Rep. **7**, 15125 (2017).

[22] R. Takagi, Y. Yamasaki, T. Yokouchi, V. Ukleev, Y. Yokoyama, H. Nakao, T. Arima, Y. Tokura, and S. Seki, Nat. Commun. **11**, 5685 (2020).

[23] B. I. Halperin and D. R. Nelson, Phys. Rev. Lett. **41**, 121 (1978).

[24] J. Zázvorka, F. Dittrich, Y. Ge, N. Kerber, K. Raab, T. Winkler, K. Litzius, M. Veis, P. Virnau, and M. Kläui, Adv. Funct. Mater. **30**, 2004037 (2020).

[25] F. Büttner, I. Lemesh, and G. S. D. Beach, Sci. Rep. **8**, 4464 (2018).

[26] Y. Zhou, R. Mansell, S. Valencia, F. Kronast, and S. van Dijken, Phys. Rev. B **101**, 054433 (2020).

[27] G. Blatter, M. V. Feigel'man, V. B. Geshkenbein, A. I. Larkin, and V. M. Vinokur, Rev. Mod. Phys. **66**, 1125 (1994).

[28] A. Thiele, Phys. Rev. Lett. **30**, 230 (1973).

[29] Y. Zhou, R. Mansell, and S. van Dijken, Sci. Rep. **9**, 6525 (2019).

[30] C. Schütte, J. Iwasaki, A. Rosch, and N. Nagaosa, Phys. Rev. B **90**, 174434 (2014).

[31] J. Miltat, S. Rohart, and A. Thiaville, Phys. Rev. B **97**, 214426 (2018).

[32] See Supplemental Material at http://link.aps.org/supplemental/10.1103/PhysRevB.106.054413 for two videos taken at position (V). Supplemental video 1 is taken at 0 mT and shows fluctuations in the stripe domains. Supplemental video 2 is taken at 0.26 mT and shows the dense skyrmion state. Supplemental video 3 shows the skyrmion state at 0.26 mT for all six positions, as labeled in the video. Supplemental video 4 shows a $300 \times 300$ pixel detail of the simulations.

[33] M. S. Pierce, J. E. Davies, J. J. Turner, K. Chesnel, E. E. Fullerton, J. Nam, R. Hailstone, S. D. Kevan, J. B. Kortright, K. Liu, L. B. Sorensen, B. R. York, and O. Hellwig, Phys. Rev. B **87**, 184428 (2013).

[34] C.-H. Sow, K. Harada, A. Tonomura, G. Crabtree, and D. G. Grier, Phys. Rev. Lett. **80**, 2693 (1998).

[35] L. Rózsa, A. Deák, E. Simon, R. Yanes, L. Udvardi, L. Szunyogh, and U. Nowak, Phys. Rev. Lett. **117**, 157205 (2016).

[36] R. Brearton, G. van der Laan, and T. Hesjedal, Phys. Rev. B **101**, 134422 (2020).

[37] A. L. Balk, M. D. Stiles, and J. Unguris, Phys. Rev. B **90**, 184404 (2014).

[38] A. Singh, J. C. T. Lee, K. E. Avila, Y. Chen, S. A. Montoya, E. E. Fullerton, P. Fischer, K. A. Dahmen, S. D. Kevan, M. K. Sanyal, and S. Roy, Nat. Commun. **10**, 1988 (2019).

[39] W. Kob and J.-L. Barrat, Eur. Phys. J. B **13**, 319 (2000).

[40] J.-H. Lee, R. Mansell, D. Petit, A. Fernández-Pacheco, R. Lavrijsen, and R. P. Cowburn, SPIN **03**, 1340013 (2013).

[41] J.-P. Bouchaud and A. Georges, Phys. Rep. **195**, 127 (1990).

[42] K. Wang, L. Qian, S.-C. Ying, G. Xiao, and X. Wu, Nanoscale **11**, 6952 (2019).

[43] G. Bourianoff, D. Pinna, M. Sitte, and K. Everschor-Sitte, AIP Adv. **8**, 055602 (2018).

[44] J. C. Phillips, Rep. Prog. Phys. **59**, 1133 (1996).

[45] R. Juge, K. Bairagi, K. G. Rana, J. Vogel, M. Sall, D. Mailly, V. T. Pham, Q. Zhang, N. Sisodia, M. Foerster, L. Aballe, M. Belmeguenai, Y. Roussigné, S. Auffret, L. D. Buda-Prejbeanu, G. Gaudin, D. Ravelosona, and O. Boulle, Nano Lett. **21**, 2989 (2021).

[46] S. Li, W. Kang, X. Zhang, T. Nie, Y. Zhou, K. L. Wang, and W. Zhao, Mater. Horiz. **8**, 854 (2021).

[47] J. Iwasaki, M. Mochizuki, and N. Nagaosa, Nat. Commun. **4**, 1463 (2013).

[48] J.-Y. Tinevez, N. Perry, J. Schindelin, G. M. Hoopes, G. D. Reynolds, E. Laplantine, S. Y. Bednarek, S. L. Shorte, and K. W. Eliceiri, Methods **115**, 80 (2017).

[49] A. Vansteenkiste, J. Leliaert, M. Dvornik, M. Helsen, F. Garcia-Sanchez, and B. Van Waeyenberge, AIP Adv. **4**, 107133 (2014).

[50] J. Mulkers, B. Van Waeyenberge, and M. V. Milošević, Phys. Rev. B **95**, 144401 (2017).

[51] J. Leliaert, B. Van de Wiele, A. Vansteenkiste, L. Laurson, G. Durin, L. Dupré, and B. Van Waeyenberge, J. Appl. Phys. **115**, 233903 (2014).

[52] D. B. Allan, T. Caswell, N. C. Keim, and C. M. van der Wel, Trackpy v0.4.2 (2019).